RSC Advances

PAPER

View Article Online
View Journal | View Issue

Cite this: *RSC Adv.*, 2026, **16**, 26173

Low-field strain-driven phase diagram of $(Bi_{1/2}Na_{1/2})TiO_3$–$SrTiO_3$–$LiNbO_3$ lead-free relaxor ceramics for actuator applications

Nguyen Hoang Thien Khoi[ab] and Nguyen Hoc Thang *[c]

This work presents the design and systematic investigation of a new ternary system, $(1-x-y)(Bi_{1/2}Na_{1/2})TiO_3$–$xSrTiO_3$–$yLiNbO_3$ (BNST100x/100yLN) ceramics, which was created to address the problems associated with high driving fields and large hysteresis in conventional $(Bi_{1/2}Na_{1/2})TiO_3$ (BNT)-based ceramics. The synthesis of these ceramics was achieved through a conventional solid-state reaction route, followed by extensive characterization regarding structural evolution, phase transition behavior, dielectric response, ferroelectric properties, and electric-field-induced strain. The addition of $LiNbO_3$ (LN) greatly accelerates the sintering behavior kinetics allowing high densification at lower temperatures while also causing an evident transition from non-ergodic relaxor (NER) to ergodic relaxor (ER) states. This transition is always confirmed by (i) strong frequency dispersion and T_m shift in dielectric spectra, (ii) progressive slimming of P–E loops with suppressed remanent polarization, and (iii) evolution of bipolar strain from butterfly-shaped to nearly linear behavior. A low-field (≤4 kV mm^{-1}) strain-driven phase diagram was constructed based on multiple quantitative criteria; it shows a systematic shift of the phase boundary toward the BNT-rich region upon LN incorporation. A broad NER-ER coexistence region has been found where an optimal balance between polarization magnitude and relaxor dynamics gives rise to a superior electromechanical response. For example, compositions like BNST24/1LN and BNST24/2LN show big reversible strains (~0.22–0.24%) with reduced hysteresis under a relatively low electric field of 4 kV mm^{-1}. The enhanced performance is due to defect-mediated polarization dynamics where Li^+/Nb^{5+} co-substitution creates oxygen vacancies and strong random fields that promote very dynamic polar nanoregions (PNRs) and flatten the free energy landscape. This finding shows that LN is acting as an effective phase-boundary engineering component instead of just being a passive dopant; thus, giving a good way toward developing high-performance low-field lead-free piezoelectric actuators.

Received 25th January 2026
Accepted 21st April 2026

DOI: 10.1039/d6ra00669h

rsc.li/rsc-advances

1. Introduction

The fast growth of piezoelectric ceramics for precision sensors, actuators, and electromechanical transducers has made the need for eco-friendly materials that can match or beat the performance of traditional lead-based systems even greater. $Pb(Zr, Ti)O_3$ (PZT) is still the best choice for industry because it has great piezoelectric coefficients and large strain response. Lead is toxic, which raises serious environmental and regulatory issues. This is why so much research is being done on lead-free alternatives.[1–3] Bismuth-based perovskite oxides, especially $(Bi_{1/2}Na_{1/2})TiO_3$ (BNT), have become one of the most promising options because they have a large spontaneous polarization, a strong electric-field-induced strain, and a high Curie temperature.[2–8] In contrast to classical ferroelectrics, the macroscopic electromechanical response in BNT-based ceramics is primarily influenced by electric-field-induced phase transitions rather than intrinsic piezoelectric coefficients related to long-range ferroelectric order. These materials are commonly designated as incipient piezoceramics.[2–5]

Even with these benefits, two big problems make it hard to use them in real life: (i) severe hysteresis from irreversible domain switching, and (ii) the need for high driving electric field (usually >6 kV mm^{-1}) to start the relaxor-to-ferroelectric phase transition.[2,9–16] These high operating fields not only waste energy, but they also make it harder to make devices smaller, keep them working a long time, but work with multilayer actuator technologies. So, a big problem in making next-generation lead-free piezoelectric actuators is getting them to

[a]*Department of Silicate Materials, Faculty of Materials Technology, Ho Chi Minh City University of Technology (HCMUT), 268 Ly Thuong Kiet Street, Dien Hong Ward, Ho Chi Minh City, Vietnam*

[b]*Vietnam National University Ho Chi Minh City, Linh Xuan Ward, Ho Chi Minh City, Vietnam*

[c]*Faculty of Chemical Engineering, Ho Chi Minh City University of Industry and Trade, 140 Le Trong Tan, Tay Thanh Ward, Ho Chi Minh City, 700000, Vietnam. E-mail: thangnh@huit.edu.vn*

work with less electric fields while still being able to handle a lot of strain. This necessitates meticulous regulation of the free-energy landscape that dictates polar nanoregions (PNRs), phase stability, and field-induced phase transitions, which continuous to be a formidable challenge in intricate perovskite systems. One of the most successful ways to lower the critical electric field in BNT-based ceramics is to make solid solutions with $SrTiO_3$ (ST). This led to the creation of $(Bi_{1/2}Na_{1/2})TiO_3$–$SrTiO_3$ (BNST) systems. Adding ST stabilizes relaxor states close to room temperature and helps core–shell microstructure form, which lowers the threshold field needed to create large strains by a lot.[17,18] To enhance phase stability and electromechanical properties, ternary modifications of BNST systems have been investigated by integrating additional perovskite components, including $BaTiO_3$ (BT), $(Bi_{1/2}K_{1/2})TiO_3$ (BKT), or $AgNbO_3$ (AN).[19–22] For instance, Zhu *et al.* reported a large strain of 0.27% at a reduced electric field of 4 kV mm^{-1} in $AgNbO_3$-modified BNST ceramics, demonstrating the effectiveness of compositional engineering in lowering the operating field.[22]

Simultaneously, lithium niobate ($LiNbO_3$, LN), a highly covalent ABO_3-type ferroelectric, has been integrated into several KNN- and BNT-based systems, demonstrating efficacy in suppressing long-range ferroelectric order while enhancing relaxor behavior.[23–27] Prior research has shown that the inclusion of LN lowers the ferroelectric-relaxor transition temperature and encourages ergodic relaxor behavior by enhancing crystallographic disorder and inducing random electric fields.[24,26,28,29] From a defect chemistry standpoint, the aliovalent substitution of Li^+ at the A-site and Nb^{5+} at the B-site is anticipated to induce charge imbalance, which can be rectified through the creation of oxygen vacancies and cation vacancies. These defect structures create local random fields that are very important for keeping dynamic PNRs stable and changing the relaxor state. Nonetheless, despite these advancements, a comprehensive understanding of the synergistic effects of ST and LN within a cohesive BNT-based ternary system is still absent. The connection between defect chemistry, low-field electromechanical response, and phase boundary evolution is still not very clear. Moreover, the majority of current research emphasizes high-field (>6 kV mm^{-1}) electromechanical responses, while low-field behavior, more pertinent to practical multilayer actuator applications, has been relatively underexplored. Moreover, previously published phase diagrams are frequently developed using qualitative criteria, which do not provide precise and uniform quantitative definitions of phase boundaries, particularly concerning the transition from non-ergodic relaxor (NER) to ergodic relaxor (ER) states.

To tackle these problems, this study presents and methodically examines a novel ternary relaxor system, $(1 - x - y)(Bi_{1/2}Na_{1/2})TiO_3$–$xSrTiO_3$–$yLiNbO_3$ (BNST100x/100yLN). Unlike earlier research that only looked at LN as a simple dopant, this shows that it can do more than one thing at once, such as changing phase stability, defect chemistry, and microstructural evolution. Specifically, the addition of LN is shown to: (i) control the defect structure through aliovalent substitution and charge compensation, which improves random fields and PNR dynamics; (ii) move the phase boundary toward the BNT-rich side, which opens up the compositional window for creating large strain, (iii) encourage liquid-phase-assisted sintering, which lowers the processing temperature and increases densification, and (iv) stabilize the ergodic relaxor state at room temperature, which allows for large reversible strain under a low electric field of 4 kV mm^{-1}. A significant contribution of this study is the development of a low-field strain-driven phase diagram founded on quantitative criteria obtained from polarization, strain, and dielectric responses. This method gives a better physical picture of how phases change than traditional high-field diagrams. This study establishes a comprehensive structure–property–performance relationship by correlating X-ray diffraction analysis, dielectric relaxation, polarization behavior, and strain response.

Although LN has been identified as a phase-boundary-regulating component in other systems, including BNT-BT and BNT-BKT,[24,30] its function in the BNST ternary system is still inadequately investigated. BNT-BT systems depend on morphotropic phase boundary effects, but BNST systems are heavily affected by A-site disorder and core–shell microstructures. This study elucidates a specific mechanism through which LN synergistically interacts with the BNST matrix to facilitate improved low-field electromechanical performance. This research illustrates that the BNST-LN ternary system serves as a promising foundation for the advancement of next-generation lead-free piezoelectric actuators, presenting a distinctive amalgamation of defect-engineered phase regulation, low-field operation, and improved strain performance.

2. Experimental procedure

2.1. Materials preparation

This study produced a series of ceramic powders made up of $(1 - x - y)(Bi_{1/2}Na_{1/2})TiO_3$–$xSrTiO_3$–$yLiNbO_3$ (denoted as BNST100x/100yLN, with x values of 0.22, 0.24, and 0.26, and y values of 0, 0.01, 0.02, and 0.03) using a standard solid-state reaction method. The raw materials used were very pure: Bi_2O_3 (99.9%), Na_2CO_3 (99%), TiO_2 (99.9%), $SrCO_3$ (99.9%), Li_2CO_3 (99.99%), and Nb_2O_5 (99.9%) (High Purity Chemicals, Japan). The initial powders were weight according to the planned stoichiometric composition and mixed in ethanol with ZrO_2 balls for 24 hours to make sure they were all mixed together evenly. The mixtures were dried and then calcined at 850 °C for 2 hours. After being heated, the powders were ball-milled in ethanol for 24 hours and then dried.

The powders were then pressed under a uniaxial pressure of 98 MPa into the pellet samples with 12 mm diameter and 2 mm thickness. To keep Bi and Na from evaporating during sintering, the pellets were buried in sacrificial powder of the same type and put in sealed alumina crucibles. Depending on the composition, sintering took place at temperatures between 1050 and 1175 °C for 2 hours. After sintering, selected samples were crushed into powders for phase analysis, and all samples were annealed at 400 °C for 30 minutes to relieve residual stress and eliminate possible oxygen vacancy gradients prior to electrical measurements.

2.2. Characterization techniques

X-ray diffraction (XRD, Ultima IV, Rigaku, Japan) with CuKα radiation ($\lambda = 1.5406$ Å) was used to look at the ceramics' phase structure. The diffraction data were gathered within a suitable 2θ range to ascertain phase purity and structural evolution. The highest intense diffraction peak was used to find out the crystallite size (D), lattice strain (ε), and dislocation density (δ). In which, the crystallite size (D) was determined *via* the Scherrer equation:

$$D = \frac{K\lambda}{\beta \cos \theta}$$

where K is the shape factor (0.9), λ is the X-ray wavelength, β is the full width at half maximum (FWHM), and θ is the Bragg angle.

In addition, the lattice strain (ε) was determined using the following equation:

$$\varepsilon = \frac{\beta}{4 \tan\theta}$$

And the dislocation density (δ) was determined as follows:

$$\delta = \frac{1}{D^2}$$

Bragg's law was used to find the lattice parameter (a) of the pseudocubic perovskite structure, and the atomic packing factor (APF) was used to measure how tightly packed the structure was. Also, the refined lattice parameter was used to figure out the lengths of the bonds between atoms, such as the distances between A and O, B and O, and A and B. This gave us an idea of how the structure was distorted in certain places.

Field-emission scanning electron microscopy (FE-SEM, JSM-6500 F, JEOL, Japan) was used to look at the microstructure of the sintered ceramics. A ferroelectric test system was used to measure the polarization–electric field (P–E) and strain–electric field (S–E) hysteresis loops at 1 Hz (aixPES, aixACCT Systems GmbH, Germany). In addition, temperature-dependent dielectric permittivity was measured using a precision LCR meter (E4980AL, Keysight, USA) over frequencies of 1 kHz, 10 kHz, and 100 kHz. The measurements were conducted in a temperature-controlled chamber with a heating rate of 2 °C min^{-1}. All electrical measurements were performed on silver-electrode samples to ensure good electrical contact and reproducibility.

3. Results and discussion

3.1. Sintering behaviors of BNST100*x*/100*y*LN ternary system *via* shrinkage and relative density

Fig. 1 illustrates how the shrinkage and relative density values of BNST100*x*/100*y*LN ceramics with different amounts of LN compare, when they are sintered at temperatures of 1050 °C and 1175 °C. The ceramics sintered at 1175 °C without any LN changes show a shrinkage rate of about 16% and a high relative density of 96–98%. On the other hand, those that were sintered at 1050 °C without LN show a much lower shrinkage rate of about 8–9%, which means that they did not get dense enough at lower temperatures. It is interesting to note that when LN is added, the samples that were sintered at 1050 °C have shrinkage rates and relative densities similar to those of the undoped samples that were sintered at the higher temperature of 1175 °C. This clearly shows that adding LN to BNST ceramics improves their sintering behavior, which makes them much denser at much lower temperatures.

The addition of LN appears to act as an effective sintering aid, promoting densification at lower temperatures. This behavior can be explained by improved mass transport processes such as lattice diffusion and grain boundary migration, which are necessary for densification.[31,32] Specifically, Li-containing species are known to promote defect-assisted diffusion, whereas Nb incorporation may modify the local bonding environment and lower diffusion barriers. Moreover, it is plausible to assert that the partial emergence of a transient liquid phase linked to Li-containing compounds (*e.g.*, Li_2CO_3-derived species) may facilitate the augmented densification behavior. This kind of sintering with the help of a liquid phase can help particles move around and speed up the movement of mass along grain boundaries. It is important to note, though, that direct microstructural evidence (like observing the phase at the grain boundary or mapping the composition) is needed to fully confirm this mechanism.

The reported enhancement in densification aligns with prior studies on BNKT-based lead-free relaxor materials, wherein the inclusion of LN similarly lowered the sintering temperatures and improved microstructural uniformity.[24] It is important to note that better densification will likely have a direct effect on electrical properties. This is because higher density lowers dielectric loss due to porosity and makes the electric field distribution more even. From a structure–property standpoint, the capacity to attain elevated density at reduced sintering temperatures is especially beneficial for regulating grain growth and defect distribution, which are essential determinants influencing relaxor behavior and electromechanical performance. So, LN not only helps with sintering, but it also plays a big role in shaping the microstructure that will affect the electrical and strain responses that will be talked about in the next sections.

3.2. Phase structure and XRD analysis

Fig. 2 shows the XRD patterns of the sintered BNST100*x*/100*y*LN ceramics with only one type of cubic perovskite structure. This is further corroborated by the lack of splitting in any peaks except $K_{\alpha 2}$, a consistent finding in other BNT-based materials.[10–14,28–31,33–36] The XRD patterns was used to evaluate for the crystallographic structure and phase evolution of the BNST100*x*/100*y*LN ceramics in a systematic way. This study focused on quantitative peak analysis to look at phase stability and structural changes caused by adding $LiNbO_3$ (LN). All compositions display a single-phase perovskite structure, indexed to a pseudocubic symmetry with space group $Pm\bar{3}m$ (No. 221), devoid of detectable secondary phases within the instrumental resolution. This observation validates the effective

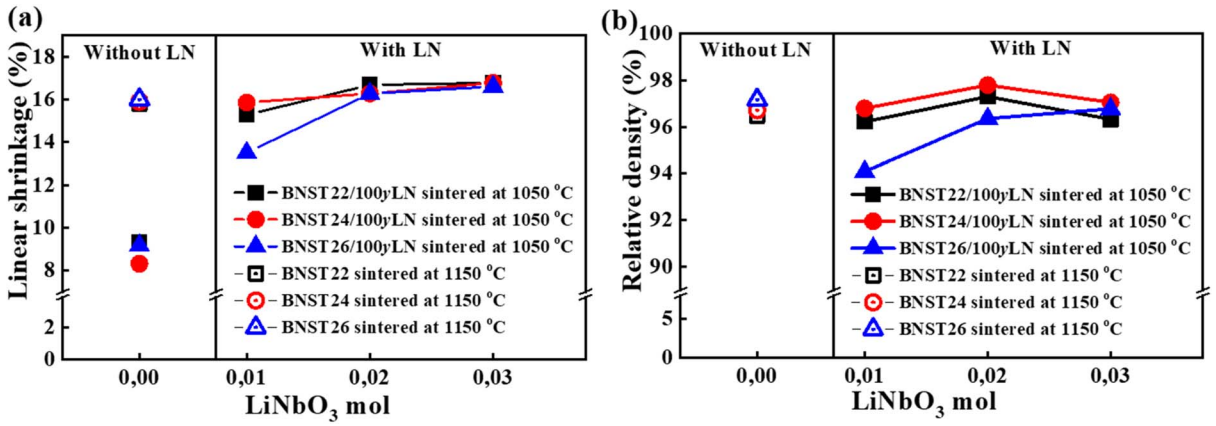

Fig. 1 (a) Linear shrinkage and (b) relative density values of BNST100*x*/100*y*LN ternary system.

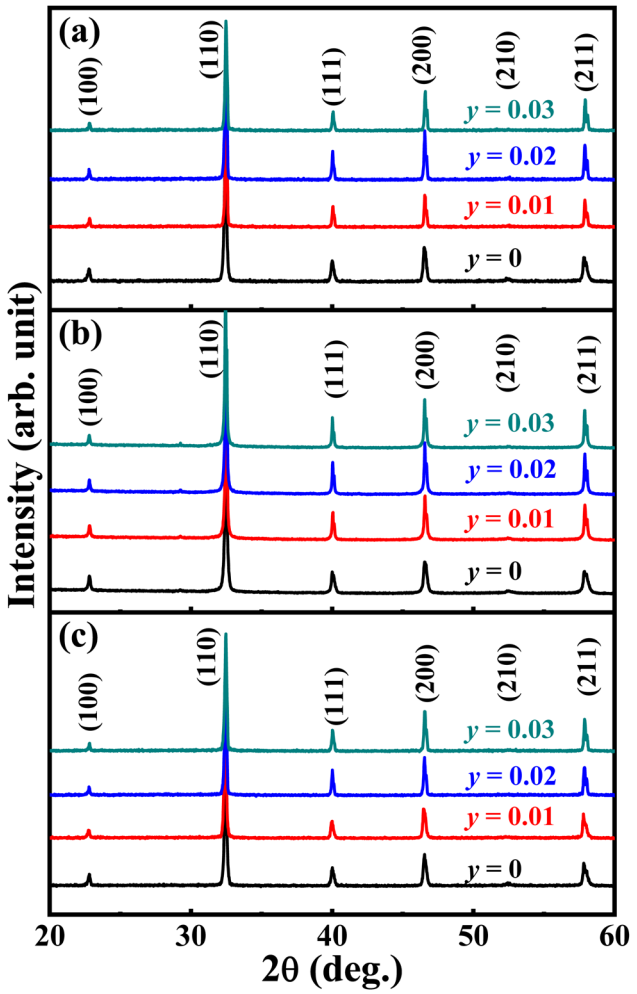

Fig. 2 XRD patterns of BNST100*x*/100*y*LN ceramics, (a) BNST22/100*y*LN, (b) BNST24/100*y*LN, and (c) BNST26/100*y*LN ceramics.

integration of $SrTiO_3$ and $LiNbO_3$ into the $(Bi_{1/2}Na_{1/2})TiO_3$ lattice, resulting in a continuous solid solution throughout the examined compositional spectrum. Instead of the usual qualitative XRD analysis, a detailed quantitative evaluation was done using the strongest diffraction peak (around $2\theta \approx 32.4°$), which is the pseudocubic (110) reflection in BNT-based systems (Fig. 3(a–c)). The structural parameters were calculated like full width at half maximum (FWHM), crystallite size (D), lattice parameter (a), lattice strain (ε), dislocation density (δ), atomic packing factor (APF), and interatomic bond lengths (L_{A-O}, L_{B-O}, and L_{A-B}) to get a better understanding of how the structure changes over time.

3.2.1 Peak characteristics and crystallite size evolution. The FWHM values drop a lot when LN is added, especially for the BNST22 and BNST24 compositions. This means that the crystals are more ordered and less disordered at the nanoscale. For instance, the FWHM goes down from 0.2240° (BNST22-000) to about 0.16–0.17° in LN-modified samples (Table 1). This means that the size of the crystallites goes up from about 36.9 nm to about 50 nm (Fig. 3(d–f)). The pattern holds true for all compositional series, which means that adding LN to the mix encourages grain growth at the crystallite level, even though SEM analysis shows that the overall grain size is getting smaller. The discrepancy between crystallite size (XRD) and grain size (SEM) suggests that LN facilitates a refined microstructure characterized by smaller grains formed from larger coherent domains. Many investigations reported about this kind of behavior in BNT-based relaxor systems, where dopants help with densification and crystallization while stopping abnormal grain growth.

3.2.2 Changes in the lattice parameter and phase boundary. The lattice parameter (a) exhibits slight yet consistent fluctuations in relation to both $SrTiO_3$ and LN content, varying from approximately 3.894 Å to 3.902 Å. Even though the change seems small, it is important for perovskite systems because even small changes in the lattice can have a big effect on polarization behavior and phase stability. When LN was added at 0.01 mol to BNST22 compositions, the lattice parameter goes down a little bit and then stays the same. This shows that the lattice is getting smaller because smaller Li^+ ions are taking the place of Ti^{4+} ions at the A-site and Nb^{5+} ions at the B-site. In contrast, BNST26 compositions show slightly larger lattice parameters (~3.898–3.902 Å) because $SrTiO_3$ is more stable in a cubic lattice. The change in lattice parameters is an

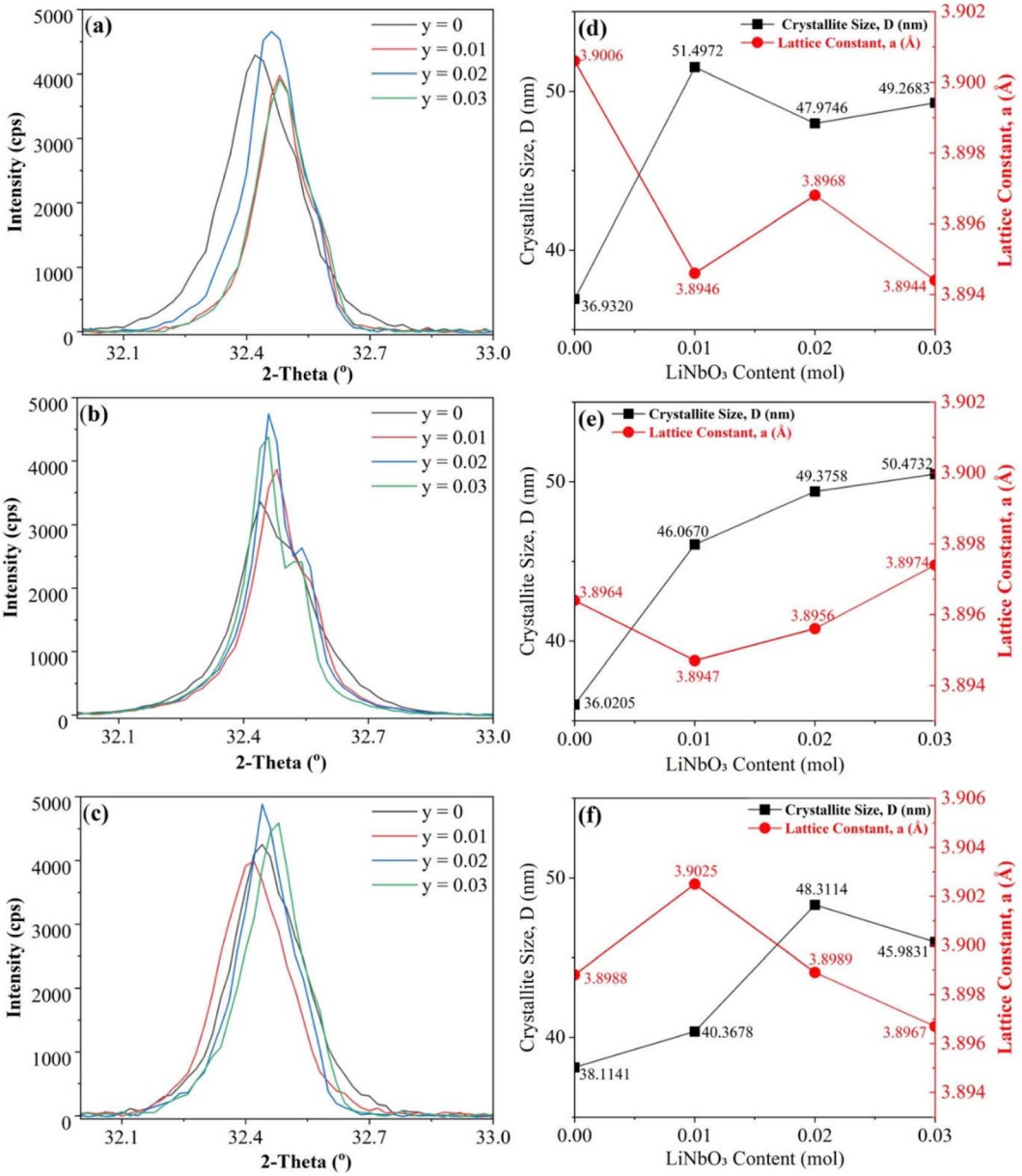

Fig. 3 The diffraction peak of (110) plane for ceramic samples of BNST 22 (a), BNST 24 (b), BNST 22 (c), and crystallite size (nm), lattice constant (Å) of ceramic samples of BNST 22 (d), BNST 24 (e), BNST 22 (f).

important piece of evidence that LN moves the phase boundary toward the BNT-rich side. The diminished lattice distortion in LN-modified BNST22 and BNST24 compositions indicates improved cubicity and the suppression of long-range ferroelectric distortion, characteristic of ergodic relaxor behavior.

3.2.3 Microstrain and structural disorder caused by defects. When LN was added, the lattice strain (ε) goes down a lot, especially in BNST22, where ε goes from about 3.36×10^{-3} to about $2.4–2.5 \times 10^{-3}$. The same thing happens in the BNST24 and BNST26 systems. This drop in microstrain shows that internal stresses are easing and the structure is becoming more uniform. Simultaneously, the dislocation density (δ) drops a lot, from about 73×10^{-3} Å^{-2} in BNST22-000 to between 37 and 43 $\times 10^{-3}$ Å^{-2} in LN-modified samples. This decrease indicates that LN functions as a defect-regulating agent, promoting defect elimination and diminishing crystallographic flaws. The addition of aliovalent ions (Li^+ and Nb^{5+}) will always cause point defects, especially oxygen vacancies ($V_O^{\cdot\cdot}$), to balance the charge. These defects cause local structural heterogeneity and random electric fields. XRD does not directly show these, but they show up as relaxor behavior in dielectric and ferroelectric measurements. So, the decrease in microstrain that was seen does not mean that there is no local disorder. Instead, it shows a change from long-range strain fields to short-range structural heterogeneity, which is in line with the formation of polar nanoregions (PNRs).

3.2.4 Atomic packing factor and bond length analysis. The atomic packing factor (APF) stays pretty much the same (~0.675–

Table 1 The structural parameters of BNST100x/100yLN ceramics calculated from XRD data with $K = 0.9$, $\lambda = 1.5406$ Å

Sample	FWHM (°)	2-Theta (°)	Crystallite size (nm)	Lattice constant, a (Å)	Lattice strain ($\varepsilon \times 10^{-3}$)	δ ($\times 10^{-3}$ Å^{-2})	APF	L_{A-O} (Å)	L_{B-O} (Å)	L_{A-B} (Bi/Na–Ti) (Å)
BSTN 22-000	0.2240	32.4347	36.9320	3.9006	3.3607	73.3154	0.6752	2.7581	1.9503	3.3780
BSTN 22-001	0.1607	32.4858	51.4972	3.8946	2.4065	37.7079	0.6783	2.7539	1.9473	3.3729
BSTN 22-002	0.1725	32.4669	47.9746	3.8968	2.5846	43.4488	0.6772	2.7555	1.9484	3.3748
BSTN 22-003	0.1680	32.4874	49.2683	3.8944	2.5152	41.1970	0.6784	2.7538	1.9472	3.3727
BSTN 24-000	0.2297	32.4709	36.0205	3.8964	3.4420	77.0729	0.6774	2.7552	1.9482	3.3744
BSTN 24-001	0.1796	32.4852	46.0670	3.8947	2.6902	47.1216	0.6783	2.7540	1.9474	3.3729
BSTN 24-002	0.1676	32.4772	49.3758	3.8956	2.5105	41.0178	0.6778	2.7546	1.9478	3.3737
BSTN 24-003	0.1639	32.4622	50.4732	3.8974	2.4570	39.2535	0.6769	2.7559	1.9487	3.3752
BSTN 26-000	0.2171	32.4499	38.1141	3.8988	3.2550	68.8379	0.6761	2.7569	1.9494	3.3765
BSTN 26-001	0.2050	32.4188	40.3678	3.9025	3.0763	61.3755	0.6742	2.7595	1.9512	3.3796
BSTN 26-002	0.1713	32.4494	48.3114	3.8989	2.5680	42.8451	0.6761	2.7569	1.9494	3.3765
BSTN 26-003	0.1799	32.4679	45.9831	3.8967	2.6965	47.2938	0.6772	2.7554	1.9484	3.3747

0.678) for all compositions. This means that the overall packing efficiency of perovskite lattice stays the same even when the composition changes. This stability shows that adding LN does not change the basic structure of the perovskite. Bond length analysis gives us more useful information. The A–O bond length (L_{A-O}) goes down a little when LN is added, which shows that smaller Li^+ ions are being added to the A-site. The B–O bond length (L_{B-O}) stays pretty stable (about 1.947–1.951 Å), which means that the octahedral framework is only slightly disturbed. On the other hand, the distance between A and B (L_{A-B}) changes slightly in ways that are related to changes in lattice parameters and phase evolution. These changes suggest that the local strain and bonding environment have been redistributed. This is very important for changing the system's free energy landscape.

3.2.5 Implications for phase evolution and relaxor behavior. The combined structural parameters give strong indirect proof that the LN caused a change in phase stability. Specifically, bigger crystallites lead to better structural coherence. Lower microstrain and dislocation density lead to better structural uniformity. A little bit of lattice contraction and bond-length change alter the polarization environment. These changes work together to stop long-range ferroelectric order and encourage the formation of PNRs that change over time. This is in line with what was seen in electrical measurements when the system went from non-ergodic relaxor (NER) to ergodic relaxor (ER) states. The lack of peak splitting in characteristic reflections like {111} and {200} is a clear sign that the structure is pseudocubic. It is important to note, though, that XRD alone may not be able to fully find small changes in the local structure of relaxor systems. Consequently, the present analysis concentrates on peak broadening, lattice parameter evolution, and derived structural parameters to deduce phase behavior.

The observed structural evolution aligns with prior findings on BNT-based ternary systems. For example, adding LN to BNT-BT and BNT-BKT systems has been shown to reduce lattice distortion and stabilize relaxor phases by increasing chemical disorder and random fields. Adding $SrTiO_3$ is also known to make cubic symmetry more likely and lower the critical field for phase transition. The BNST-LN ternary system shows a more gradual and controllable change in structure than these other systems. This is shown by the systematic changes in lattice parameters and microstrain. This indicates that LN functions not only as a dopant but also as a phase-boundary regulator, facilitating precise adjustments to the energy landscape. The current XRD analysis offers significant insights into structural evolution; however, it is recognized that additional methods, including Raman spectroscopy, or transmission electron microscopy, would yield more direct evidence of local structural heterogeneity and phase coexistence. These methods are suggested for subsequent research to enhance the validation of the proposed mechanism. Quantitative XRD analysis verifies that all BNST100x/100yLN ceramics retain a single-phase pseudocubic perovskite structure while demonstrating systematic structural evolution upon LN incorporation. The decrease in microstrain and dislocation density, along with slight changes to the lattice and bond lengths, strongly suggests that LN affects the stability of phases. These structural changes explain the change from non-ergodic to ergodic relaxor behavior and back up the idea that the phase boundary is moving toward the BNT-rich area.

3.3. Microstructure evolution and grain size analysis

Fig. 4 shows the polished and thermally etched surfaces of the BNST100x/100yLN ceramics. For pure BNST without LN modification (Fig. 4(a–c)), the samples display dense microstructures featuring well-defined grains and grain boundaries, signifying efficient densification at elevated sintering temperatures. It is well known that the BNT-based ceramics usually densify best between 1150 °C and 1200 °C[10,28,33,34] which is what this study was conducted. Dense microstructures are also seen in LN-modified BNST ceramics (Fig. 4(d–l)), even in samples that were sintered at lower temperatures. This confirms that adding LN makes sintering much better, as the shrinkage and density results already showed. However, it is important to note that achieving complete densification in BNT-based ceramics at lower temperatures typically necessitates improved mass transport mechanisms.

The presence of Li-containing species is linked to the role of LN in encouraging densification. It is hypothesized that Li_2CO_3

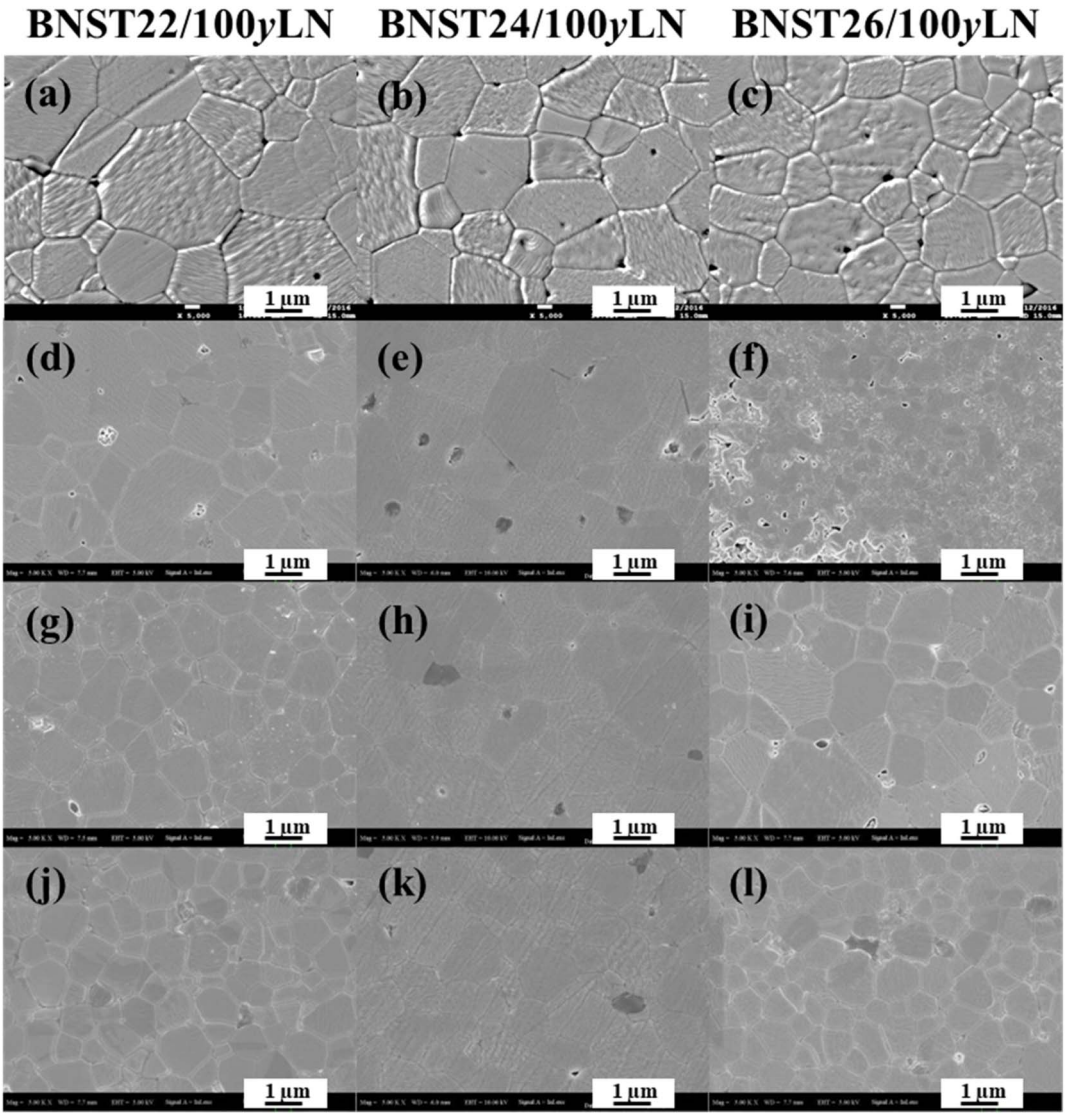

Fig. 4 Polished and thermally-treated surface images of BNST100*x*/100*y*LN ternary, (a–c) $y = 0$, (d–f) $y = 0.01$, (g–i) $y = 0.02$, (j–l) $y = 0.03$.

acts as a raw precursor, breaks down into Li_2O and CO_2 at high temperatures by the following reaction: $Li_2CO_3 \xrightarrow{\sim 740^\circ C} Li_2O + CO_2\uparrow$, with Li_2O may act as a fluxing agent that helps mass transport.[34] In this case, LN may facilitate a liquid-phase-assisted sintering (LPS) process that improves the rearrangement of particles and the diffusion of grain boundaries. Nonetheless, it is crucial to underscore that direct microstructural evidence of a residual liquid phase (*e.g.*, grain boundary films or compositional segregation) is absent in the current SEM images. Consequently, LPS is regarded as a plausible contributing mechanism rather than a definitive conclusion, in alignment with prior reports.[33] One thing that stands out about the microstructure is that the grain size get smaller as the LN content goes up. Quatitative grain size analysis (based on statistical measurements from multiple SEM images) shows that the average grain size for BNST22/100*y*LN decreased consistently from 4.25 μm to 1.6 μm with increasing LN content. The BNST24/100*y*LN and BNST26/100*y*LN compositions also show a similar trend of decreasing, which shows that adding LN has a general effect of refining grains.

The smaller grains have a big effect on how the ceramics work. Smaller grains naturally make the density of grain boundaries higher. These boundaries act as mechanical barriers to the movement of domain walls and make long-range ferroelectric domains less stable. From a thermodynamic point of view, the increased interfacial energy and mechanical clamping effects break the continuity of polarization, which makes it more likely that nanoscale polar regions will form. As a result, grain size refinement and the chemical disorder caused by aliovalent Li^+ and Nb^{5+} substitution work together to break up large ferroelectric domains into dynamic polar nanoregions (PNRs). This microstructural confinement effect is very important for keeping the ergodic relaxor state stable. So, the decrease in grain size that was seen is not just a microstructural effect of adding LN; it is also a key factor in the change from non-ergodic relaxor (NER) to ergodic relaxor (ER) behavior. This transition is directly associated

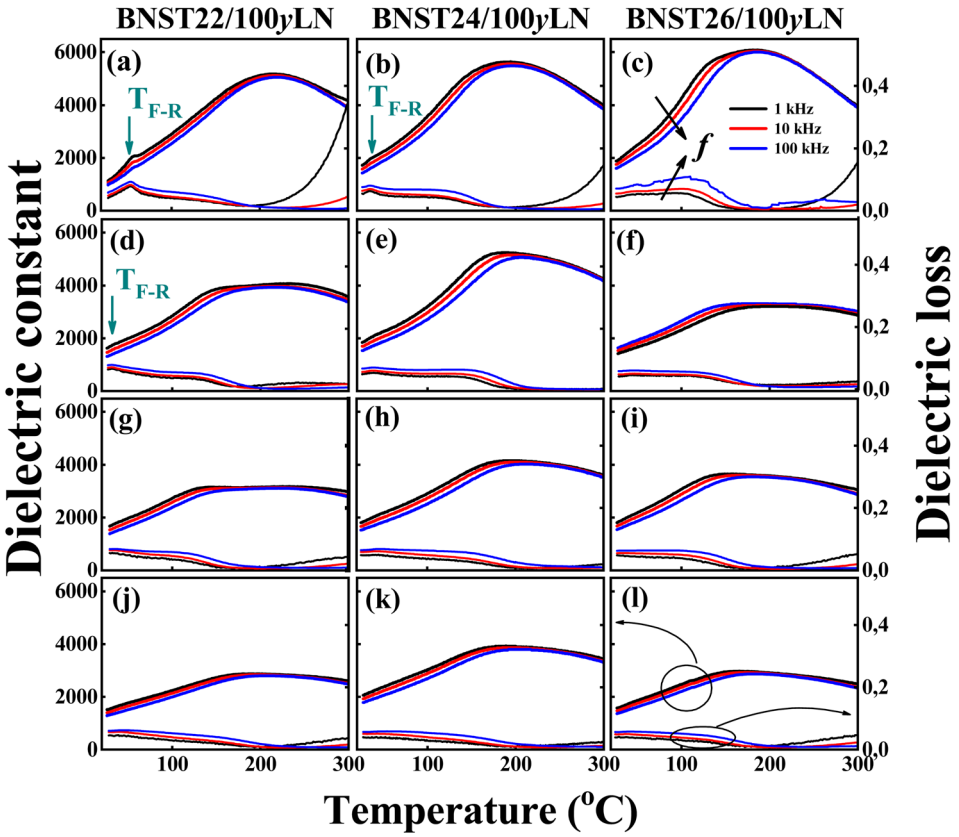

Fig. 5 Temperature-dependent permittivity (ε_r) and dielectric loss (tan δ) of the BNST100x/100yLN ceramics, (a–c) $y = 0$, (d–f) $y = 0.01$, (g–i) $y = 0.02$, (j–l) $y = 0.03$.

with the improved low-field strain response noted in the BNST-LN system, as elaborated in subsequent sections.

3.4. Dielectric properties and relaxor behavior

The temperature-dependent permittivity (ε_r) and dielectric loss (tan δ) of BNST100x/100yLN ceramics are shown in Fig. 5. All the samples have a very large frequency dispersion, which is usually found in relaxor ferroelectrics. As seen clearly from Fig. 5(a–l), the curves of dielectric permittivity give a broad maximum, and the related peak temperature (T_m) moves to higher temperatures with an increase in measurement frequency (from 1 kHz to 100 kHz). This shift of T_m with frequency is a typical feature of relaxors and indicates that there are polar nanoregions (PNRs) having a wide range of relaxation times. For the undoped compositions ($y = 0$, Fig. 4(a–c)), a relatively sharp dielectric peak is observed, indicating that more pronounced ferroelectric character has limited relaxor dispersion. As LN content increases from $y = 0.01$ to $y = 0.03$ in figures d through l, the dielectric peaks broaden progressively and become more diffuse along with increasing frequency dispersion. This evolution indicates a gradual transition from long-range ferroelectric ordering toward a relaxor state dominated by dynamic PNRs. The transition temperature from ferroelectric (FE) to relaxor (RE), referred to as T_{F-R} in BNST100x/100yLN ceramics decreases systematically with increasing LN content. The specific T_{F-R} values for BNST22, BNST24, and BNST22/1LN ceramics are approximately 54 °C, 35 °C, and 32 °C, respectively. No distinct, T_{F-R} anomaly can be noted for the compositions of BNST26/100yLN ceramics modified with LN or those with BNST24 compositions modified by LN or even for the composition of BNST22 having more than 1 mol% of LN content. This means that T_{F-R} has shifted below room temperature for these compositions indicating a fully ergodic relaxor state at ambient conditions.

Alongside the shift in T_{F-R}, systematically reduced peak sharpness and enhanced frequency dispersion with increasing LN content further confirm strengthening of relaxor behavior. Broadening dielectric peaks as well as suppression characteristics of distinct phase-transition signatures indicate reduced polarization correlation length and increased local structural heterogeneity. The dielectric characteristics at the microscopic level are basically the same as those from compositional disorder and defect-induced random fields due to aliovalent Li^+ and Nb^{5+} substitution. These effects interrupt long-range ferroelectric ordering and encourage the formation of nanoscale PNRs that can respond dynamically to external electric fields. The enhanced dynamics of PNRs allow reversible polarization switching, which is necessary to achieve large electrostrain under low electric fields. So, the decrease in T_{F-R} observed and also the enhanced frequency dispersion show that LN incorporation changes the dielectric response of BNST ceramics by inducing a transition from an ergodic relaxor (ER) state to

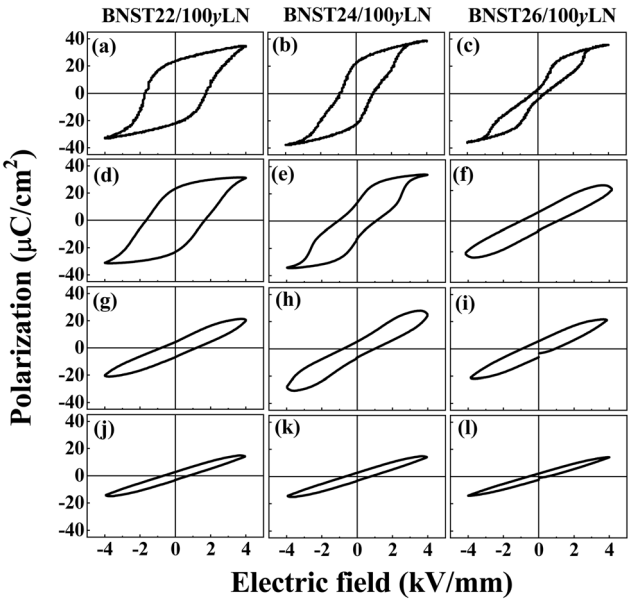

Fig. 6 Polarization hysteresis loops (*P*–*E*) of the BNST100*x*/100*y*LN ceramics, (a–c) $y = 0$, (d–f) $y = 0.01$, (g–i) $y = 0.02$, (j–l) $y = 0.03$.

a non-ergodic relaxor (NER) state near or below room temperature. This behavior has been observed and consistent with previously in dopant-modified BNT-based systems[10,13,33–35,37,38] and serves as strong dielectric evidence for phase evolution and strain behavior discussed in later sections.

3.5. Ferroelectric properties and polarization evolution

Fig. 6 illustrates the polarization hysteresis (*P*–*E*) loops of BNST100*x*/100*y*LN ceramics under an electric field of 4 kV mm^{-1}. The derived parameters, including maximum polarization (P_{max}), remanent polarization (P_r), and coercive field (E_C), are listed in Table 2. For the undoped BNST22 ceramic (Fig. 6(a)), a well-saturated ferroelectric loop was observed with P_{max}, P_r, and E_C values of ≈34 μC cm^{-2}, ≈23 μC cm^{-2}, and ≈1.7 kV mm^{-1}, respectively. This indicates that a stable non-ergodic relaxor (NER) state with long range ferroelectric ordering exists. As LN is introduced, the systematic evolution of *P*–*E* loops characterized by progressive loop slimming, reduced hysteresis, and decreasing P_r, and E_C takes place. Specifically, BNST22/2LN (Fig. 6(g)) shows a greatly narrowed hysteresis loop with P_r falling down to about 5 μC cm^{-2} and E_C much lower than before (0.12 kV mm^{-1}). It should be noted though that this composition still has some remanent polarization and weak hysteresis opening, meaning it does not completely convert into a normal ergodic relaxorER state. The presence of leftover ferroelectric features together with relaxor-like slim behavior indicates that BNST22/2LN sits in an intermediate phase region between where non-ergodic relaxor (NER) and ergodic relaxor (ER) states coexist.

More LN addition (for instance, BNST22/3LN, Fig. 5(j)) leads to very nearly linear *P*–*E* loops with almost negligible P_r, which mean that which means that a fully ergodic relaxor state has been achieved. The same trend in development can be noticed in the case of BNST24/100*y*LN ceramics; here, one can see a gradual transformation from a clearly defined hysteresis loop into narrow almost linear dependence with increasing content of LN. For BNST26/100*y*LN (Fig. 6(c, f, i and l)), the *P*–*E* loops is already pinched at low P_r and E_C values of ∼4.7 μC cm^{-2} and ∼0.4 kV mm^{-1}, respectively, for the un-doped composition of BNST26. This indicates that the system is basically close to an ergodic relaxor (ER) state; thus, adding LN will further suppress remanent polarization response. The systematic transition from square-like ferroelectric loops to slim linear ones for all compositions is a clear proof of an actual compositional change from NER to coexistence to ER states. It matches perfectly with dielectric results (Fig. 5); that is, T_{F-R} progressively decreases while frequency dispersion increases, meaning long-range ferroelectric order destabilizes and dynamic polar nano-regions (PNRs) develop.

From defect chemistry, the stabilization of the ER state when $LiNbO_3$ is added can be understood through the synergistic actions of Li^+ and Nb^{5+} substitution. Li^+ ions take up part of the A-site (replacing Bi^{3+}/Na^+/Sr^{2+}) and Nb^{5+} replaces Ti^{4+} at the B-site ($Nb_{Ti}^{\bullet}$). This aliovalent co-doping creates local charge imbalance and defect dipoles which can be balanced by oxygen vacancies and/or local lattice distortions. These defects produce random electric fields that prevent long-range ferroelectric ordering. Consequently, the polarization coherence length is shortened to a large extent; this means that macroscopic ferroelectric domains will be fragmented into nanoscale PNRs. It will be more so with grain size refinement (as seen in SEM analysis), whereby an increase in grain boundary density applies mechanical constraints on the growth of domains. The joint actions of chemical disorder and microstructural confinement flatten the free energy landscape, thus reducing the energy barrier for polarization reorientation. The coexistence behavior that has been discussed above for BNST22/2LN may simply be viewed as a transitional state wherein partially frozen PNRs (NER-like) coexist with dynamic PNRs (ER-like). These PNRs under an applied electric field of 4 kV mm^{-1} can

Table 2 Derived parameters from polarization and strain curves for the BNST100*x*/100*y*LN ceramics

	BNST22/100*y*LN				BNST24/100*y*LN				BNST26/100*y*LN			
y	0	0.01	0.02	0.03	0	0.01	0.02	0.03	0	0.01	0.02	0.03
P_{max} (μC cm^{-2})	34	31	21	14	38	34	28	15	35	23	21	14
P_r (μC cm^{-2})	23	23	5	3.4	24	14	5.9	2.9	4.7	5.6	5.3	2.2
E_c (kV mm^{-1})	1.7	1.6	1.2	0.7	0.9	0.9	0.8	0.6	0.4	0.8	0.6	0.4
S_{max} (%)	0.09	0.12	0.23	0.05	0.12	0.24	0.22	0.05	0.25	0.22	0.18	0.05
S_{max}/E_{max} (pm V^{-1})	225	300	575	125	300	600	550	125	625	550	450	150

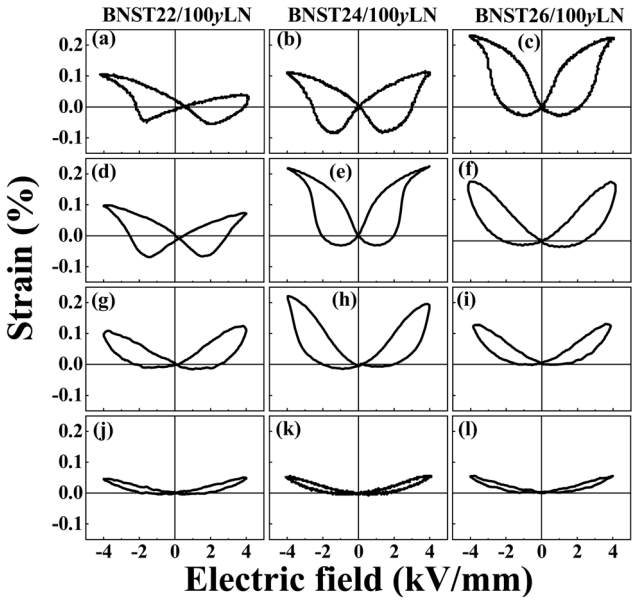

Fig. 7 Bipolar electric-field-induced strain (*S*–*E*) curves of the BNST100*x*/100*y*LN ceramics, (a–c) $y = 0$, (d–f) $y = 0.01$, (g–i) $y = 0.02$, (j–l) $y = 0.03$.

reversibly reorient but do not form stable long-range domains; hence, hysteresis is reduced and reversibility is enhanced. Thus, this loop evolution, from saturated ferroelectric to slim relaxor behavior, is direct experimental evidence for the LN-induced transition from NER to ER states. Such a transition is very important in getting large reversible strain at low electric fields since it involves field-induced polarization reconfiguration instead of irreversible domain switching.

3.6. Strain behavior and low-field electromechanical performance

Fig. 7 presents the bipolar electric-field-induced strain (*S*–*E*) loops of BNST100*x*/100*y*LN ceramics measured at an applied electric field of 4 kV mm^{-1}. In this work, the term "low-field" refers to an electric field that is less than or equal to 4 kV mm^{-1}, which is much lower than the normal operating fields for conventional BNT-based ceramics (greater than 6 kV mm^{-1}). This particular range of fields has relevance when considering practical multilayer actuator applications where reduced driving voltage would enhance reliability and allow for miniaturization of devices. For the compositions of BNST22/100*y*LN (Fig. 7(a, d, g and j)), the un-doped sample with $y = 0$ exhibits a typical butterfly-shaped *S*–*E* loop with large negative strain; this is representative of NER behavior related to ferroelectric domain switching under the influence of an electric field. On introducing LN at $y = 0.01$, the negative strain reduces slightly, indicating partial destabilization of long-range ferroelectric domains. At $y = 0.02$, the shape of the loop changes towards a more shallower butterfly form, which indicates that relaxor behavior has started. For $y = 0.03$, the *S*–*E* loop becomes almost linear with very little negative strain, which shows that it is changing to an ergodic relaxor state where reversible polarization processes dominate.

The same butterfly-to-linear evolution occurs in BNST24/100*y*LN ceramics (Fig. 7(b, e, h and k)). The un-doped sample BNST24 sample shows a strong ferroelectric response with large negative strain. With the addition of LN at $y = 0.01$, the strain behavior starts to change towards something more relaxor-like, characterized by less hysteresis and higher maximum strain. The most important result here is that at $y = 0.02$, BNST24/2LN reaches its highest maximum strain value under 4 kV mm^{-1}, reaching approximately 0.23%, with significantly suppressed negative strain indicating an optimal balance between polarization magnitude and reversibility corresponding to a transitional state between NER and ER phases. The un-doped BNST26/100*y*LN ceramics as shown in Fig. 7(c, f, i and l) already reveal weak butterfly characteristics and low negative strain, hence proving their proximity to the ergodic relaxor state as confirmed by *P*–*E* loop analysis. With increasing LN content, *S*–*E* loops become more linear, and maximum strain, reduces slightly indicating stabilization of a fully ER state with reduced polarization amplitude.

From a structure–property point of view, the change from butterfly-shaped to almost linear *S*–*E* loops represent a basic shift in how strain is caused-from irreversible domain switching (NER state) to reversible PNR reorientation (ER state). This transition matches perfectly with the dielectric results (decreasing T_{F-R}) and the *P*–*E* loop evolution (loop slimming), confirming the progressive stabilization of the ergodic relaxor state with increasing LN content. Therefore, in compositions like BNST24/2LN where enhanced strain response is seen, it can be attributed to an optimal coexistence of polar order and disorder, where enough polarization is kept while greatly lowering the energy barrier for polarization switching. This allows large reversible strain at low electric fields and makes the BNST-LN system very promising for next generation low voltage piezoelectric actuator applications.

3.7. Low-field strain-driven phase diagram

The low-field strain driven phase diagram of BNST100*x*/100*y*LN ceramics is shown in Fig. 8, which was develop through an in-depth integration of dielectric, polarization, and strain responses measured at a maximum electric field of 4 kV mm^{-1}. The phase diagram is different from traditional ones that are established under high electric fields (>6 kV mm^{-1}) because it aims to reflect realistic opening conditions for multilayer actuators. Therefore, it constitutes a more application-relevant framework for assessing the stability of phases and the performance in electromechanics for BNT-based systems. An important aspect of the proposed phase diagram is that it shows a systematic movement of the morphotropic phase boundary toward the side rich in BNT with increasing ln content. This change clearly proves that ln does not just act as a passive dopant but plays an active role in stabilizing the ergodic relaxor (ER) state. This migration of phase boundaries fully agrees with what has been observed structurally and microstructurally and described in earlier sections. Specifically, XRD analysis revealed

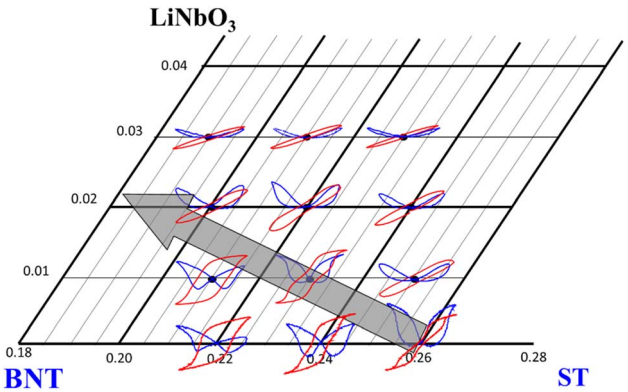

Fig. 8 Phase diagram based on strain and polarization behaviors of BNST100*x*/100*y*LN ternary system in the range of 0.20–0.26 mol ST content.

increased lattice disorder and subtle lattice contraction; SEM results demonstrated significant grain size refinement, and dielectric as well as polarization measurements confirmed the suppression of long-range ferroelectric ordering. These combined effects promote dynamically reconfigurable polar nanoregions (PNRs), which are stabilized by ER phases.

For qualitative and possibly inconsistent phase classification, the phase boundaries in Fig. 8 were determined based on a set of five mutually consistent quantitative criteria derived from convergent electromechanical signatures. First, remanent polarization (P_r) was used as a primary indicator; values greater than ~10 μC cm^{-2} would correspond to non-ergodic relaxor (NER) behavior while those below ~5 μC cm^{-2} would indicate ER characteristics. Second, substantial reduction in coercive field (E_c), especially below ~1 kV mm^{-1}, was taken as evidence for enhanced relaxor behavior due to lowered domain-switching barriers. Third, the morphology of the *P*–*E* hysteresis loops was interpreted in detail, where saturated loops are NER states, slim and almost linear loops are ER states, and pinched loops represent intermediate or coexistence behavior. Fourth, the presence or absence of negative strain in bipolar *S*–*E* curves was taken as a structural marker: pronounced negative strain means NER; vanishing negative strain means ER; partial negative strain indicates transitional states. The normalized strain response (S_{max}/E_{max}) was used finally to pick out the high-performance region, with peak values in the range of ~500–700 pm V^{-1} corresponding to compositions very close to the phase boundary. These criteria applied together make sure that the phase diagram is based not on one parameter but on a strong and reproducible multi-parameter framework responding to rigor and consistency among the properties.

One of the most important improvements made in this work is clearly identifying an explicit coexistence region between classical NER and ER phases as shown in Fig. 9. This intermediate region corresponds to an energy landscape where long-range ferroelectric domains coexist with dynamic PNRs (Fig. 9). The composition BNST22/2LN that previously looked

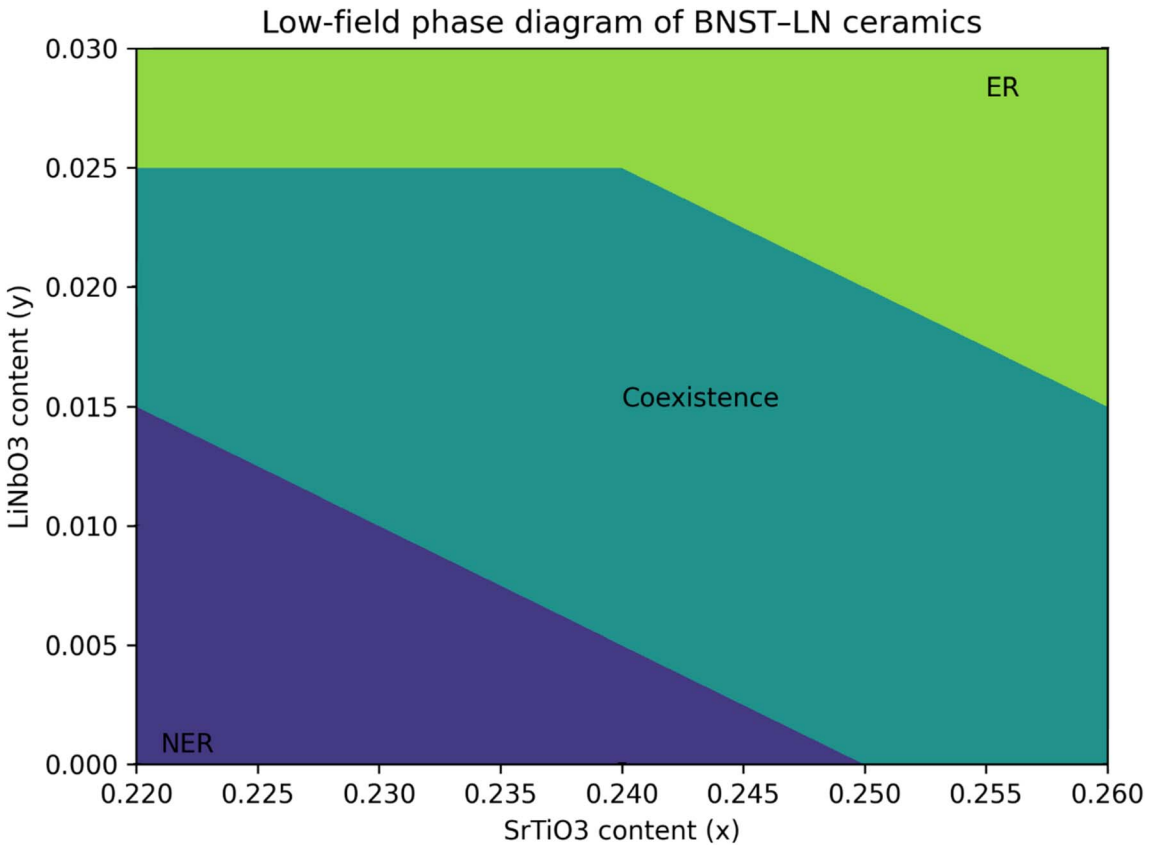

Fig. 9 Low-field (4 kV mm^{-1}) phase diagram of BNST-LN system.

inconsistent when judged by individual measurements gets very clear identification here for belonging to this coexistence region. Its hybrid electromechanical response strongly supports this classification: the *P–E* loop shows a highly pinched and narrowed shape typical of ER behavior while in the corresponding *S–E* curve there is still some residual negative strain which indicates an NER character. Also, this composition has an intermediate remanent polarization value ($P_r \approx 5$ μC cm^{-2}) exactly at the boundary between two regimes. This confirms that BNST22/2LN is indeed a mixed state system with dynamic PNRs dominating under low fields but where a small fraction of frozen ferroelectric domains still contributes to strain hysteresis. The inclusion of this coexistence region addresses the discrepancies and gives a physically meaningful explanation for transitional compositions.

The phase diagram captures the compositional evolution from NER to ER behavior with increasing LN content, following the path NER to coexistence to ER as shown in Fig. 9. Increasing $SrTiO_3$ (ST) content (x) also stabilizes ER but through a different mechanism involving lattice softening and core–shell microstructure formation. The combination of ST and LN moves ferroelectric-to-relaxor transition temperature (T_{F-R}) down below room temperature, increases chemical disorder and random electric fields, and stabilizes highly dynamic PNRs. More importantly, LN moves the phase boundary toward lower ST content so that ER behavior can be achieved in more BNT-rich compositions. This is good because it means that the system can keep fairly high polarization levels while also lowering the needed operating electric field. A broad high-strain compositional window is clearly delineated within the phase diagram under a low-field condition of 4 kV mm^{-1}. It is this region that we have highlighted in Fig. 8, and it corresponds to compositions with a maximum strain (S_{max}) of ≥0.22%, which is actually critical for actuator applications. The best compositions lie in between BNST24/1LN and BNST24/2LN, while BNST22/2LN happens to be at the edge of this high-performance area. Herein, S_{max} attains some value between 0.22–0.24%, and normalized strain response goes up to about ~550–600 pm V^{-1}, when hysteresis has been much reduced as compared with classical ferroelectric compositions; that means better performance due to an optimal balance between structural instability permitting large strain generation and ergodic relaxor dynamics ensuring reversibility under low electric fields.

The phase diagram is valid based on the unipolar strain behavior in Fig. 10. In the NER region, unipolar *S–E* curves show almost linear behavior at low strain values (~0.09–0.12%), indicating that conventional domain switching mechanisms dominate. The coexistence compositions have the largest strain values (~0.23–0.24%) (Table 2), proving that maximum electromechanical response takes place close to the phase boundary. For fully developed ER region compositions, an even larger drop in strain response (~0.05%) indicates suppression of polarization magnitude despite highly reversible PNR dynamics; this trend strongly experimentally validates that the coexistence region is indeed optimal for balancing polarization magnitude and reversibility. From a mechanism point of view, it is field-induced reconfiguration of polar nanoregions that governs enhanced strain performance in the coexistence region rather than irreversible ferroelectric domain switching. The addition of LN brings in considerable defect chemistry and lattice disorder which together flatten free-energy landscapes and reduce energy barriers between different polarization states. As such, PNRs become very dynamic and can now respond reversibly to electric fields as small as ≤4 kV mm^{-1}. This mechanism can account for the simultaneous reduction in hysteresis, increase in energy efficiency, and improvement of strain reversibility seen in optimized compositions. It would also imply better fatigue resistance and cycling stability which are very important for practical actuator applications.

Finally, Table 3 shows how the BNST-LN system's electromechanical performance compares to that of the best BNT-based ceramics. The current system attains a substantial strain of approximately 0.22–0.24% at a modest electric field of 4 kV mm^{-1}. This performance is comparable to $AgNbO_3$-modified BNST systems (around 0.27% at 4 kV mm^{-1}) and markedly exceeds that of conventional BNT-BT systems,[39–41] which generally necessitate significantly higher fields (about 7 kV mm^{-1}) to reach similar strain levels.[30] The normalized strain (~600 pm V^{-1}) is also very competitive, and the compositional tolerance is much wider. These results clearly show that LN works not only as a dopant but also as an effective phase-boundary engineering component. This makes it possible to make high-performance, low-field actuators in BNT-based ceramics.

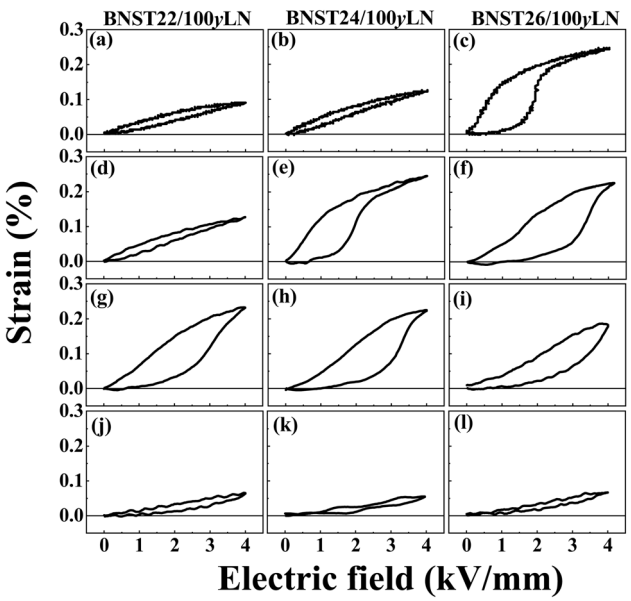

Fig. 10 Unipolar electric-field-induced strain curves of the BNST100*x*/100*y*LN ceramics, (a–c) $y = 0$, (d–f) $y = 0.01$, (g–i) $y = 0.02$, (j–l) $y = 0.03$.

3.8. Defect chemistry and mechanism

To describe the basic source of the seen shift from non-ergodic relaxor to ergodic relaxor behavior in BNST-LN ceramics, it is necessary to create a defect-chemistry-driven framework that

Table 3 Comparison of electromechanical strain performance in recent lead-free BNT-based ceramics

System	S_{max}	E_{max}	Normalized strain (S_{max}/E_{max})	Reference
$AgNbO_3$-modified 0.76BNT-0.24ST (BNST-AN)	0.27%	4 kV mm^{-1} (40 kV cm^{-1})	~700 pm V^{-1}	38
La_2CoMnO_6-modified BNT-BT6.5 (BNT-BT-LCMO)	0.22%	7 kV mm^{-1} (70 kV cm^{-1})	328 pm V^{-1}	39
MnO_2-modified BNT-24ST	0.18%	2 kV mm^{-1}	902 pm V^{-1}	40
Pure BNT-BT with LN doping	0.60%	7 kV mm^{-1} (70 kV cm^{-1})	~857 pm V^{-1}	30
(BNT-ST)-LN	~0.24%	4 kV mm^{-1}	~600–700 pm V^{-1}	This study

consistently links aliovalent substitution, lattice disorder, polarization dynamics, and macroscopic electromechanical response. In the current system, the addition of $LiNbO_3$ introduces simultaneous A-site and B-site substitutions that greatly change the local charge balance and structural heterogeneity of the perovskite lattice. These defect-mediated changes are key in making long-range ferroelectric order unstable and allowing relaxor behavior under low electric fields. From a crystallographic view, the parent BNST system has a cubic perovskite structure where the A-site is statistically filled by Bi^{3+}, Na^+, and Sr^{2+} ions while Ti^{4+} sits at the B-site. With LN added, Li^+ ions mostly take up space at A-site; Nb^{5+} replaces Ti^{4+} at B-site. This dual-site aliovalent substitution creates a significant local charge imbalance that needs compensation for maintaining overall electroneutrality. In oxide ceramics processed at high temperatures, such compensation is usually achieved through the formation of oxygen vacancies even though A-site vacancies and defect associations might contribute locally. Within Kröger–Vink notation, this can be described as coexistence between donor-type defects ($Nb_{Ti}^{\bullet}$) and acceptor-type defects ($Li_A^{'}$), with oxygen vacancies ($V_O^{\bullet}$) being the main charge compensators.

The formation of oxygen vacancies is further enhanced by Bi and Na volatility during sintering as well as the existence of Li-containing precursors which lead to local non-stoichiometry. This means that BNST-LN lattice turns out to be a very defect-rich system with strong local electrostatic inhomogeneity. These charged defects and their spatial distribution create very strong random electric fields that prevent dipoles from aligning cooperatively needed for long-range ferroelectric order to set up. Instead of macroscopic ferroelectric domains, the system prefers the emergence of nanoscale correlated polarization regions known as polar nanoregions (PNRs). The strength and spatial distribution of these random fields are directly governed by the concentration of aliovalent dopants (Li^+ and Nb^{5+}), the density of oxygen vacancies, and intrinsic A-site compositional disorder in BNT-based systems. In BNST-LN ceramics, it is a highly heterogeneous electrostatic landscape that exists due to multi-valence A-site cations ($Bi^{3+}/Na^+/Sr^{2+}/Li^+$) together with B-site substitution (Nb^{5+}/Ti^{4+}). Such an environment reduces significantly the correlation length of polarization and favors dynamically fluctuating PNRs. This behavior perfectly agrees with enhanced frequency dispersion in dielectric measurements and progressively reducing ferroelectric-relaxor transition temperature (T_{F-R}) as LN content increases.

The transition from NER to ER behavior can therefore be interpreted as a direct consequence of increasing defect-induced disorder and the associated evolution of PNR dynamics. In the NER state, PNRs are relatively large and partially frozen at room temperature, requiring a sufficiently high electric field to align into long-range ferroelectric domains. This results in characteristic features such as saturated or pinched *P–E* loops, large remanent polarization, and pronounced negative strain in bipolar *S–E* curves. However, as the LN content increases, the density of defects and random fields becomes sufficiently high to fragment these PNRs into smaller highly dynamic entities; thus, the system enters an ER state where PNRs may reversibly reorient under low electric fields without establishing stable long-range order. This evolution is experimentally evidenced by transforming *P–E* loops systematically from saturated to slim and nearly linear shapes with marked reductions in remanent polarization and coercive field plus disappearance of negative strain in *S–E* curves. From this perspective, the transition induced by defects can be viewed as a gradual flattening of the free energy landscape. In classical ferroelectrics, the free energy profile has deep and well-defined minima corresponding to stable polarization states, separated by high energy barriers. However, when compositional disorder and defect dipoles are introduced into the BNST-LN system, these energy barriers become significantly reduced resulting in a shallow highly degenerate energy landscape. The resulting flattening of the landscape allows continuous rotation of polarization and redistribution among many local minima which gives rise to large electromechanical responses at substantially lower electric fields. This means that the strain mechanism changes from irreversible domain switching towards reversible field-induced reconfiguration of PNRs – a hallmark feature of relaxor ferroelectrics.

This mechanism is consistent with the enhanced low-field strain performance observed in compositions located near the NER-ER boundary such as BNST24/1LN and BNST24/2LN. The composition achieves an optimal balance between residual polarization magnitude and dynamic relaxor behavior in these materials; hence large reversible strain (about 0.22% to 0.24%) can be generated at just 4 kV mm^{-1} with very little hysteresis. It should be noted that this behavior agrees with phase diagram analysis since coexistence region corresponds to flattened free energy landscape enabling efficient field-induced polarization reconfiguration. Further insight into the defect-structure–property relationship can be obtained by correlating these findings with structural results and microstructural results presented earlier. The XRD analysis indicates a stable cubic average structure with subtle variations in lattice parameters and reduced microstrain which suggest long-range structural distortion suppression. Observations from SEM systematically show

decreasing grain size as more LN content is added; this increases grain boundary density thus introducing more mechanical constraints that destabilize ferroelectric domain formation even further. Defect-induced random fields synergistically enable formation of highly dynamic PNRs under such microstructural conditions. Simultaneously, dielectric data show strong frequency dispersion and the downward shift of T_{F-R}, while polarization and strain data indicate a gradual transition from ferroelectric-like to relaxor-like behavior. These results provide strong experimental support for the proposed defect-mediated mechanism. It should also be emphasized that the transition from NER to ER happens over a finite compositional range; hence there is a coexistence region characterized by mixed polarization states. An exemplary case is BNST22/2LN, which shows both ER-like slim *P–E* loops and residual NER-like negative strain. This apparent contradiction can be rationalized in terms of spatial heterogeneity in defect distribution and local structure that leads to regions with different degrees of stabilization for the polarization. In such compositions, dynamic PNRs dominate the polarization response under low fields, while a fraction of frozen domains persists and contributes to strain hysteresis. This coexistence state corresponds to a transitional free energy landscape and plays an important role in achieving maximum electromechanical performance.

While this defect chemistry model provides a physically consistent interpretation of what has been observed, it can be noted that this is primarily inferred from macroscopic measurements. Direct characterization techniques such as transmission electron microscopy, Raman spectroscopy, or synchrotron-based local structure analysis would give more insight into the spatial distribution of defects and PNRs. However, strong correlation between structural, dielectric, polarization, and strain data gives much credence to the proposed mechanism. $LiNbO_3$ doping in BNST ceramics leads to aliovalent Li^+/Nb^{5+} substitutions creating oxygen vacancies with strong random electric fields that inhibit long-range ferroelectric order and facilitate dynamic polar nanoregions. This disorder induced by defects flattens the free energy landscape allowing reversible polarization reconfiguration as well as large strain under low electric fields. The resulting transition from NER to ER behavior provides a robust mechanistic basis for the enhanced low-field electromechanical performance observed in the BNST-LN ternary system.

3.9. Structure–property–performance correlation

To fully grasp the improved low-field electromechanical response in BNST-LN ceramics, it is essential to create a single correlation that connects crystallographic structure, defect chemistry, polarization dynamics, and macroscopic strain behavior. In this system, such a connection can be coherently built by linking structural features revealed through X-ray diffraction (XRD) with defect-induced local heterogeneity, formation and evolution of polar nanoregions (PNRs), and finally the observed strain performance under low electric fields. XRD analysis shows that all compositions studied crystallize into one-phase pseudocubic perovskite with space group $Pm\bar{3}m$; therefore, secondary phases are absent proving that $LiNbO_3$ has been successfully incorporated into BNST lattice. Though this structural simplicity seems apparent, detailed quantitative analysis brings out subtle but significant changes in lattice parameters, lattice strain and crystallite size with varying LN content. The progressive reduction of lattice strain and dislocation density along with the stabilization of the lattice parameter is indicative of long-range lattice distortion being suppressed. It is a transition from relatively distorted ferroelectric framework to more symmetric pseudocubic configuration. Such transition should not be understood as an increase in conventional ferroelectric order but rather weakening long-range polar coupling while short-range correlations still exist and are preserved. This interpretation gets further support from microstructural observations where grain size refinement together with increased grain boundary density introduces additional constraints for extended ferroelectric domains to develop. Hence, the XRD-derived structural evolution establishes the first critical step in the correlation, namely transforming the lattice from a long-range ordered ferroelectric state to a structurally averaged but locally heterogeneous relaxor framework.

Building on this structural skeleton, defect chemistry takes center stage in controlling the local polarization map. The addition of $LiNbO_3$ brings aliovalent substitutions at both the A and B sites, with Li^+ taking the place of $Bi^{3+}/Na^+/Sr^{2+}$ and Nb^{5+} substituting for Ti^{4+}. This substitution at two different sites creates a local charge imbalance that is mainly balanced by oxygen vacancy formation during processing at high temperatures. The resulting defect complexes together with intrinsic A-site compositional disorder provide very strong local electrostatic fluctuations usually referred to as random fields. These random fields disrupt coherence over long ranges for dipole alignment and prevent stabilization of macroscopic ferroelectric domains; instead, the system prefers forming nanoscale regions of correlated polarization called polar nanoregions. The strength of such random fields increases with LN content since more PNRs form as indicated by increased frequency dispersion in dielectric measurements plus a continuous drop in remanent polarization and coercive field seen from *P–E* loops. Therefore, what structural evolution was found by XRD should be interpreted together with defect chemistry: an apparent reduction in lattice distortion actually corresponds not to a more ordered ferroelectric state but rather a transition toward some defect-dominated locally heterogeneous environment favoring PNR formation.

The dynamic behavior of these PNRs under an applied electric field provides the direct link between microscopic structure and macroscopic electromechanical response. In compositions located within the non-ergodic relaxor regime, PNRs are relatively large and partially frozen at room temperature, requiring substantial electric fields to align into long-range ferroelectric domains. This results in characteristic features such as saturated or pinched *P–E* loops and pronounced negative strain in bipolar *S–E* curves. However, as the LN content increases, the enhanced defect-induced random fields reduce the correlation length of PNRs and increase their

dynamic nature. In this ergodic relaxor regime, PNRs can easily reorient and redistribute under relatively small electric fields without developing a stable long-range order. This transition is very much reflected in the change of electromechanical behavior, where the butterfly-shaped strain loops gradually become almost linear and reversible responses with a big reduction in hysteresis. The maximum electromechanical response occurs close to the NER-ER boundary because here there is an optimal balance between the size of residual polarization and mobility of PNRs. In this coexistence region, the system has enough polarization to produce large strain, while the flattened energy landscape allows fast and reversible field-induced reconfiguration of PNRs.

From a thermodynamic point of view, this can be explained by thinking about how the free energy landscape gets more and more flat because of defect chemistry and structural disorder. In normal ferroelectrics, deep energy wells keep different polarization states stable because they are separated by high barriers; thus, domain switching is irreversible with high hysteresis. On the other hand, BNST-LN has a shallow and very degenerate energy landscape where many polarization states are separated by low energy barriers. This flattening makes it easy for continuous polarization rotation and redistribution among PNRs under low electric fields to allow large reversible strain. The link between PNR dynamics and strain response is therefore direct and basic: more dynamic and weakly correlated PNRs mean better conversion of electrical energy into mechanical deformation under low-field conditions.

The structure–property–performance relationship integrated in this study can therefore be described as an ongoing, mutually dependent sequence. A pseudocubic framework with suppressed long-range distortion is defined by structural evolution derived from XRD; defect chemistry introduces oxygen vacancies along with strong random fields that destabilize long-range ferroelectric order; these random fields assist the dynamic behavior and formation of PNRs; finally, field-induced reconfiguration of PNRs controls macroscopic strain response. This is a unified framework that is entirely in agreement with the experimental findings through various characterization techniques regarding the decrease in lattice strain, grain structure refinement, increased dielectric dispersion, narrowing of *P–E* loops, and change from butterfly-type to reversible strain behavior.

Significantly, this correlation gives a direct clear design principle for improving low-field actuator performance. The BNST-LN system does not use the conventional morphotropic phase boundary systems which depend mainly on crystallographic phase coexistence but rather employs defect-mediated polarization dynamics in order to obtain an excellent electromechanical response. By adjusting aliovalent substitution and defect concentration, the system can be brought into the NER-ER coexistence region where structural instability and dynamic polarization interplay for maximum strain at reduced electric fields. This method increases electromechanical performance, widens compositional tolerance, and improves processing reliability as well as scalability for real-world applications. The low-field strain enhancement in BNST-LN ceramics results from a synergistic interaction between structural evolution, defect chemistry, and PNR dynamics. The transition from long-range ferroelectric order to a dynamically disordered relaxor state allows efficient and reversible electromechanical coupling at low electric fields which gives solid physical consistency for the next generation of lead-free piezoelectric actuators.

4. Conclusion

This work provides a detailed study of the structural, dielectric, ferroelectric, and electromechanical properties of $(1-x-y)(Bi_{1/2}Na_{1/2})TiO_3$–$xSrTiO_3$–$yLiNbO_3$ (BNST100x/100yLN) ceramics with an emphasis on low-field strain performance and phase evolution. The simultaneous incorporation of $SrTiO_3$ (ST) and $LiNbO_3$ (LN) into the BNT matrix has been demonstrated as an effective method for tuning the balance between ferroelectric order and relaxor behavior. The main discovery is that the addition of LN causes a gradual shift in the morphotropic phase boundary toward the BNT-rich side, which coincides with a clear transition from non-ergodic relaxor to ergodic relaxor states. This transition is always supported by dielectric dispersion behavior, lowering of ferroelectric-relaxor transition temperature (T_{F-R}), gradual narrowing of *P–E* hysteresis loops, and changes in strain responses from butterfly-type to almost linear characteristics. The enhanced relaxor behavior is fundamentally governed by defect chemistry associated with Li^+/Nb^{5+} co-substitution which creates oxygen vacancies and strong random fields; these two factors disrupt long-range ferroelectric order and promote dynamic polar nanoregions (PNRs). The free energy landscape flattens so that reversible polarization reconfiguration can happen under low electric fields.

A low-field strain-driven phase diagram generated with multiple quantitative criteria defines phase boundaries in a physically robust way. A separate NER-ER coexistence region is reported where compositions such as BNST22/2LN show mixed behavior and serve as a transition boundary. It is within this region that the polarization and relaxor dynamics compete optimally to give the maximum electromechanical response. The best performance among all compositions is seen for BNST24/1LN and BNST24/2LN, which achieve large reversible strain (~0.24%) at a relatively low electric field of 4 kV mm^{-1} with less hysteresis. The present BNST-LN ceramics compare favorably in terms of the strain levels achieved as compared to previously reported BNT-based systems; they do so under lower operating fields and with better compositional tolerance. This work establishes LN incorporation as an efficient pathway for phase-boundary engineering and defect-mediated property tuning in BNT-based ceramics. The results presented herein offer a firm basis for the future design of next-generation lead-free piezoelectric materials with high strain output under practical low-field conditions.

Conflicts of interest

There are no conflicts to declare.

Data availability

All processed data supporting the main findings, such as XRD patterns, SEM images, electrical measurements (strain-electric field, polarization-electric field), and derived parameters, are fully presented in the main article and the accompanying supplementary information (SI). Supplementary information is available. See DOI: https://doi.org/10.1039/d6ra00669h.

Availability of additional data: the raw and supporting datasets are available from the corresponding author upon reasonable request. The data can be shared for academic and research purposes, provided that appropriate context and collaboration are ensured to avoid misinterpretation of complex measurement conditions. Conditions and limitations: there are no ethical or commercial restrictions on data sharing. However, due to the specialized nature of the measurement systems and data processing procedures, we recommend that requests include sufficient detail regarding intended use so that we can provide appropriate guidance alongside the data.

Acknowledgements

We acknowledge the support of time and facilities from Ho Chi Minh City University of Technology (HCMUT), VNU-HCM for supporting this study.

References

1 J. Rödel, W. Jo, K. T. P. Seifert, E.-M. Anton, T. Granzow and D. Damjanovic, *J. Am. Ceram. Soc.*, 2009, **92**(6), 1153–1177, DOI: 10.1111/j.1551-2916.2009.03061.x.

2 W. Jo, R. Dittmer, M. Acosta, J. Zang, C. Groh, E. Sapper, K. Wang and J. Rödel, *J. Electroceram.*, 2012, **29**(1), 71–93, DOI: 10.1007/s10832-012-9742-3.

3 J. Rödel, K. G. Webber, R. Dittmer, W. Jo, M. Kimura and D. Damjanovic, *J. Eur. Ceram. Soc.*, 2015, **35**(6), 1659–1681, DOI: 10.1016/j.jeurceramsoc.2014.12.013.

4 C.-H. Hong, H.-P. Kim, B.-Y. Choi, H.-S. Han, J.-S. Son, C.-W. Ahn and W. Jo, *J. Materiomics*, 2016, **2**(1), 1–24, DOI: 10.1016/j.jmat.2015.12.002.

5 C.-W. Ahn, C.-H. Hong, B.-Y. Choi, H.-P. Kim, H.-S. Han, Y.-H. Hwang, W. Jo, K. Wang, J.-F. Li and J.-S. Lee, *J. Korean Phys. Soc.*, 2016, **68**(11), 1481–1494, DOI: 10.3938/jkps.68.1481.

6 J. Koruza, A. J. Bell, T. Frömling, K. G. Webber, K. Wang and J. Rödel, *J. Materiomics*, 2018, **4**(1), 13–26, DOI: 10.1016/j.jmat.2018.02.001.

7 M. Pandiyarajan, G. Manobalaji, M. Senthilkumar, S. M. Babu and S. Subashchandran, *Mater. Res. Express*, 2019, **6**(6), 066418, DOI: 10.1088/2053-1591/ab103d.

8 R. Subagyo, A. Arramel, L. J. Diguna, A. L. Ivansyah, M. E. Witkowski, M. Makowski, D. Kowal, W. Drozdowski, M. D. Birowosuto and Y. Kusumawati, *Mater. Res. Express*, 2022, **9**(9), 096202, DOI: 10.1088/2053-1591/ac9270.

9 X.-Y. Tong, H.-L. Li, J.-J. Zhou, H. Liu and J.-Z. Fang, *Ceram. Int.*, 2016, **42**, 16153–16159, DOI: 10.1016/j.ceramint.2016.07.133.

10 H.-S. Han, W. Jo, J.-K. Kang, C.-W. Ahn, I.-W. Kim, K.-K. Ahn and J.-S. Lee, *J. Appl. Phys.*, 2013, **113**(15), 154102, DOI: 10.1063/1.4801893.

11 T. Li, X. J. Lou, X. Q. Ke, S. D. Cheng, S. B. Mi, X. J. Wang, J. Shi, X. Liu, G. Z. Dong, H. Q. Fan, Y. Z. Wang and X. L. Tan, *Acta Mater.*, 2017, **128**, 337–344, DOI: 10.1016/j.actamat.2017.02.037.

12 C. Wang, X. Lou, T. Xia and S. Tian, *Ceram. Int.*, 2017, **43**, 9253–9258, DOI: 10.1016/j.ceramint.2017.04.081.

13 T.-H. Dinh, J.-K. Kang, J.-S. Lee, N. H. Khansur, J. Daniels, H.-Y. Lee, F.-Z. Yao, K. Wang, J.-F. Li, H.-S. Han and W. Jo, *J. Eur. Ceram. Soc.*, 2016, **36**(14), 3401–3407, DOI: 10.1016/j.jeurceramsoc.2016.05.044.

14 Q. Li, S. Gao, L. Ning, H. Fan, Z. Liu and Z. Li, *Ceram. Int.*, 2017, **43**, 5367–5373, DOI: 10.1016/j.ceramint.2017.01.084.

15 H. Zhang, P. Xu, E. Patterson, J. Zang, S. Jiang and J. Rödel, *J. Eur. Ceram. Soc.*, 2015, **35**(9), 2501–2512, DOI: 10.1016/j.jeurceramsoc.2015.03.012.

16 P. Fan, Y. Zhang, Q. Zhang, B. Xie, Y. Zhu, M. A. Mawat, W. Ma, K. Liu, J. Xiao and H. Zhang, *J. Eur. Ceram. Soc.*, 2018, **38**(13), 4404–4413, DOI: 10.1016/j.jeurceramsoc.2018.05.028.

17 M. Acosta, L. A. Schmitt, L. Molina-Luna, M. C. Scherrer, M. Brilz, K. G. Webber, M. Deluca, H.-J. Kleebe, J. Rödel and W. Donner, *J. Am. Ceram. Soc.*, 2015, **98**(11), 3405–3422, DOI: 10.1111/jace.13853.

18 J. Koruza, V. Rojas, L. Molina-Luna, U. Kunz, M. Duerrschnabel, H.-J. Kleebe and M. Acosta, *J. Eur. Ceram. Soc.*, 2016, **36**(4), 1009–1016, DOI: 10.1016/j.jeurceramsoc.2015.11.046.

19 S. Praharaj, D. Rout, S.-J. L. Kang and I.-W. Kim, *Mater. Lett.*, 2016, **184**, 197–199, DOI: 10.1016/j.matlet.2016.08.076.

20 F. Wang, M. Xu, Y. Tang, T. Wang, W. Shi and C.-M. Leung, *J. Am. Ceram. Soc.*, 2012, **95**(6), 1955–1959, DOI: 10.1111/j.1551-2916.2012.05119.x.

21 K. Wang, A. Hussain, W. Jo and J. Rödel, *J. Am. Ceram. Soc.*, 2012, **95**(7), 2241–2247, DOI: 10.1111/j.1551-2916.2012.05162.x.

22 P. Fan, Y. Zhang, S.-T. Zhang, B. Xie, Y. Zhu, M. A. Marwat, W. Ma, K. Liu, L. Shu and H. Zhang, *J. Materiomics*, 2019, **5**(3), 480–488, DOI: 10.1016/j.jmat.2019.01.004.

23 P. Wannasut, P. Jaita, A. Watcharapasorn and S. Jiansirisomboon, *Integr. Ferroelectr.*, 2016, **175**(1), 1–8, DOI: 10.1080/10584587.2016.1199238.

24 J. Hao, W. Bai, W. Li, B. Shen and J. Zhai, *J. Appl. Phys.*, 2013, **114**, 044103, DOI: 10.1063/1.4816047.

25 H. Du, F. Tang, D. Liu, D. Zhu, W. Zhou and S. Qu, *J. Mater. Sci. Eng. B*, 2007, **136**, 165–169, DOI: 10.1016/j.mseb.2006.09.031.

26 J.-U. Rahman, A. Hussain, A. Maqbool, R. A. Malik, T.-K. Song, M.-H. Kim, S.-H. Lee and W.-J. Kim, *J. Korean Phys. Soc.*, 2015, **66**(5), 661–666, DOI: 10.3938/jkps.66.661.

27 Z.-Y. Shen, Y.-M. Li, L. Jiang, R.-R. Li, Z.-M. Wang, Y. Hong and R.-H. Liao, *J. Mater. Sci.: Mater. Electron.*, 2011, **22**, 1071–1075, DOI: 10.1007/s10854-010-0261-1.

28 R. A. Malik, A. Hussain, A. Maqbool, A. Zaman, C.-W. Ahn, J.-U. Rahman, T.-K. Song, W.-J. Kim and M.-H. Kim, *J. Am.*

Ceram. Soc., 2015, **98**(12), 3842–3848, DOI: 10.1111/jace.13722.

29 A. Zaman, A. Hussain, R. A. Malik, A. Maqbool, S.-H. Nahm and M.-H. Kim, *J. Phys. D: Appl. Phys.*, 2016, **49**, 175301, DOI: 10.1088/0022-3727/49/17/175301.

30 J. Chen, Y. Wang, Y. Zhang, Y. Yang and R. Jin, *J. Eur. Ceram. Soc.*, 2017, **37**(6), 2365–2371, DOI: 10.1016/j.jeurceramsoc.2017.02.009.

31 J.-S. Kim, A. Hussain, M.-H. Kim, T.-K. Song, S.-T. Chung, C.-H. Chung and H.-S. Lee, *J. Korean Phys. Soc.*, 2012, **61**(6), 951–955, DOI: 10.3938/jkps.61.951.

32 F.-S. Tang, H.-L. Du, Z.-M. Li, W.-C. Zhou, S.-B. Qu and Z.-B. Pei, *Trans. Nonferrous Met. Soc. China*, 2006, **16**, s466–s469, DOI: 10.1016/S1003-6326(06)60235-5.

33 Y.-H. Hong, H.-S. Han, G.-H. Jeong, Y.-S. Park, T.-H. Dinh, C.-W. Ahn and J.-S. Lee, *Ceram. Int.*, 2018, **44**(17), 21138–21144, DOI: 10.1016/j.ceramint.2018.08.156.

34 H.-S. Han, D.-J. Heo, T.-H. Dinh, C.-H. Lee, J.-K. Kang, C.-W. Ahn, V.-D. N. Tran and J.-S. Lee, *Ceram. Int.*, 2017, **43**(10), 7516–7521, DOI: 10.1016/j.ceramint.2017.03.038.

35 J. Hao, W. Bai, W. Li, B. Shen and J. Zhai, *J. Appl. Phys.*, 2013, **114**(4), 044103, DOI: 10.1063/1.4816047.

36 A. Zaman, A. Hussain, R. A. Malik, A. Maqbool, S.-H. Nahm and M.-H. Kim, *J. Phys. D: Appl. Phys.*, 2016, **49**, 175301, DOI: 10.1088/0022-3727/49/17/175301.

37 H.-S. Han, W. Jo, J. Rödel, I.-K. Hong, W.-P. Tai and J.-S. Lee, *J. Phys.: Condens. Matter*, 2012, **24**, 365901, DOI: 10.1088/0953-8984/24/36/365901.

38 Y. Ehara, N. Novak, S. Yasui, M. Itoh and K. G. Webber, *Appl. Phys. Lett.*, 2015, **107**, 262903, DOI: 10.1063/1.4938759.

39 Y. Zhu, Y. Zhang, B. Xie, P. Fan, M. A. Marwat, W. Ma, C. Wang, B. Yang, J. Xiao and H. Zhang, *Ceram. Int.*, 2018, **44**(7), 7851–7857, DOI: 10.1016/j.ceramint.2018.01.220.

40 R. Cheng, Y. Zhu, L. Zhu, Z. Xu, R. Chu, J. Hao, J. Du and G. Li, *Ceram. Int.*, 2015, **41**(10), 14124–14129, DOI: 10.1016/j.ceramint.2015.07.033.

41 X.-Y. Tong, Z.-Z. Du, Y.-T. Yang, M.-W. Song, J.-J. Zhou, H.-B. Zhang, C.-L. Guan, H. Liu and J.-Z. Fang, *J. Alloys Compd.*, 2021, **857**(15), 158237, DOI: 10.1016/j.jallcom.2020.158237.